Maliha Yel Mahi
Department of Mechanical Engineering,
University of North Dakota,
Grand Forks, ND 58202-8359
e-mail: mzy0035@auburn.edu

Emmanuel Chukwuemeka
Department of Mechanical Engineering,
University of North Dakota,
Grand Forks, ND 58202
e-mail: emmanuel.chukwuemeka@und.edu

Shaun Donovan
Department of Mechanical Engineering,
University of North Dakota,
Grand Forks, ND 58202
e-mail: shaun@spdonovan.com

Forrest Ames[1]
Faculty Member
Department of Mechanical Engineering,
University of North Dakota,
Grand Forks, ND 58201
e-mails: forrest.ames@und.edu;
forrest.ames@engr.und.edu

Yousef Kanani
Department of Mechanical, Materials and
Aerospace Engineering,
Illinois Institute of Technology,
Chicago, IL 60601
e-mail: ykanani@hawk.iit.edu

Sumanta Acharya
Faculty Member
Department of Mechanical, Materials and
Aerospace Engineering,
Illinois Institute of Technology,
10 West, 32nd Street,
Chicago, IL 60601
e-mail: sacharya1@iit.edu

The Influence of Turbulence and Reynolds Number on Endwall Heat Transfer in a Vane Cascade

Endwall heat transfer measurements have been acquired in a vane cascade over a range of turbulence conditions and Reynolds numbers using an array of small commercial infrared (IR) cameras. The linear cascade was tested over five inlet turbulence conditions ranging from low turbulence (0.7%) to high turbulence (17.4%) and three exit chord Reynolds numbers ranging from 500,000 to 2,000,000. The small commercial IR cameras made by Therm-App have a resolution of 384 by 288 pixels and were connected to individual smartphones to record the images. The cascade was modified with small zinc selenide windows to provide IR access for the cameras. The five cameras were calibrated against a constant temperature test plate and the output images were adjusted for the fisheye effect and thermal droop at the edges. The large-scale low-speed cascade, used in the endwall heat transfer study, was configured in a four-vane three full passage arrangement. The vane design includes a large leading and aft loading. This same cascade has been used in the acquisition of vane surface heat transfer distributions, vane suction surface heat transfer visualizations, and vane surface film cooling distributions. This paper includes comparisons with two large eddy simulation calculations, which were conducted prior to the acquisition of the heat transfer data. The influence of the secondary flows on the endwall heat transfer distributions, including the leading edge horseshoe vortex system, is particularly visible at lower turbulence levels and lower Reynolds numbers. However, at higher turbulence levels, the influence of secondary flows is less visible but the influence of Reynolds number and turbulence on transition can be discerned. [DOI: 10.1115/1.4056778]

Keywords: fluid dynamics and heat transfer phenomena in compressor and turbine components of gas turbine engines, heat transfer and film cooling

Introduction

Land-based gas turbine systems can achieve single-digit NOx emissions using lean burning combustion systems. At the same time, rising turbine entry temperatures improve both turbine and overall cycle efficiency. However, this combination of lean burning combustion systems and higher but more-uniform turbine entry temperatures limit the air available for endwall cooling. The resulting temperature profiles also increase heat loads on the endwalls resulting in a more difficult endwall cooling problem.

Propulsion gas turbines have a greater focus on robust operability than emissions but have similar issues concerning endwall cooling. Aero-engines often generate high levels of large-scale turbulence in their compact high-intensity combustion systems resulting in further complications in assessing and dealing with the endwall cooling problem. Consequently, turbine cooling specialists need to have robust endwall heat transfer predictive methods in order to develop and assess endwall cooling approaches. The robust validation of a computational method for the prediction of endwall heat transfer, requires assessment over a range of Reynolds numbers, turbulence conditions, and preferably geometries.

The research documented in the present paper provides heat transfer predictive specialists with a comprehensive endwall heat transfer database. The present heat transfer visualizations were acquired in a large vane cascade test section, which has previously been the subject of midline and full surface vane heat transfer research. Additionally, predictions using wall-resolved LES (large eddy simulation) were conducted for a low and higher turbulence level at the lowest Reynolds number. The cascade vane profile has a large leading edge with an aft-loaded profile. The trailing edge was designed for trailing edge discharge and is thicker than a vane with a trailing edge cutback. The current endwall heat transfer data were acquired over a wide range of conditions. The Reynolds number was varied over a four-to-one range (500,000 to 2,000,000) and five distinct turbulence conditions were developed ranging from low turbulence (0.7%) to very high turbulence (17.4%). The present research is expected to be highly useful for predictive comparisons in the grounding of endwall heat transfer predictive tools.

Background

Turbine entry nozzles are designed to turn and accelerate flow into the first-stage blade row. As the inlet flow approaches the

[1]Corresponding author.

Contributed by the International Gas Turbine Institute (IGTI) of ASME for publication in the Journal of Turbomachinery. Manuscript received September 26, 2022; final manuscript received January 18, 2023; published online February 10, 2023. Tech. Editor: David G. Bogard.

vane row, it begins to encounter some strong pressure gradients. The resulting transition from the entry flow to the flow over the endwalls in the vane passage produces some complex flows often called secondary flows. Earlier, Sieverding [1] provided a comprehensive review of secondary flows on turbine passage endwalls. He presented the secondary flow models of both Klein [2] and Langston et al. [3]. Sieverding identifies Klein as first to mention a stagnation point vortex. Klein identified both a leading edge horseshoe vortex and a passage vortex. Langston's model included the main vortex systems which identified the pressure side and suction side legs of the horseshoe vortex as well as corner vortices. Sieverding acknowledges the work of Graziani et al. [4] in showing this leading edge vortex system is associated with elevated levels of heat transfer. Marchal and Sieverding [5] used a light sheet method with smoke wires and agreed with the Langston model suggesting the pressure leg of the horseshoe vortex merged with the passage vortex but identified the counter-rotating suction leg on top of the passage vortex. Langston [6] later reviewed the literature on secondary flows since Sieverding's [1] review and included the findings of Sharma and Butler [7], Goldstein and Spores [8], and Wang et al. [9]. Sharma and Butler [7] identified a counter vortex wrapping around the passage vortex. Goldstein and Spores [8] found evidence of a small intense vortex at the leading edge. Wang et al. [9] further investigated the endwall flow using laser sheets and smoke wires but at low Reynolds numbers identifying a horseshoe vortex system which was periodically varying and similar to the leading edge horseshoe vortex reported by Praisner and Smith [10,11]. Praisner and Smith investigated a leading edge horseshoe vortex system to a cylinder in crossflow at an approach Reynolds number of 24,400. They reported a time mean flow field with horseshoe, secondary, tertiary, and corner vortices. They found a peak level of heat transfer at the downwash of their horseshoe vortex and a secondary peak at the location of their secondary vortex. However, the time-varying system showed a notable level of unsteadiness.

Endwall heat transfer measurements have been documented in the literature over both vane and blade endwalls. Generally, endwall heat transfer studies show elevated heat transfer in the stagnation region and downstream off the pressure surface. Vane endwall heat transfer studies include investigations by York, et al. [12], Harasgama and Wedlake [13], and Spencer et al. [14]. However, these investigations produced results visualized with a limited number of contour lines in a single passage, which limited the ease of tying endwall heat transfer to the secondary flows. Radomsky and Thole [15] investigated endwall heat transfer using a constant heat flux technique with an infrared camera. They produced heat transfer visualizations of two full passages at low (0.6%) and high (19.5%) inlet turbulence levels. They took complementary flow field measurements with laser Doppler velocimetry (LDV) and found inlet augmentation levels of 40% and downstream augmentation levels of around 10%. They reported an inlet Reynolds number based on a chord length of 230,000 for an unconventional vane with a turning angle of 72 deg. Ames et al. [16] acquired endwall heat transfer measurements in a linear cascade at exit chord Reynolds numbers of 500,000, 1,000,000, and 2,000,000 at low (0.7%) and mock aero-combustor (13.4%) turbulence levels. They used a constant heat flux technique and mapped endwall heat transfer contours using a narrow-band liquid crystal. Ames et al. [17] made similar measurements for a mock catalytic combustor (1.5%) and a mock dry low NOx combustor (14.3%) turbulence. Generally, in addition to significant heat transfer levels in the leading edge region and downstream off the pressure surface, the data showed a movement of transition forward in the passage with increasing Reynolds number. Blade endwall heat transfer studies include studies by Goldstein and Spores [8] using naphthalene sublimation and by Giel et al. [18] in NASA's Transonic Blade Cascade Facility. Goldstein and Spores investigated the influence of boundary layer thickness and Reynolds number on heat transfer. Giel et al. investigated a highly turning blade design at low and high turbulence levels, two transonic Mach numbers, and a two-to-one range in Reynolds numbers.

The present endwall heat transfer paper contributes to a series of experimental and computational investigations. Varty and Ames [19] document vane midline heat transfer distributions for the current cascade. Varty et al. [20] document full surface vane suction surface heat transfer distributions. Kanani et al. [21] use wall-resolved LES to predict vane pressure surface heat transfer levels over a range of turbulence levels. Kanani et al. [22] use wall-resolved LES to predict bypass transition on the vane suction surface for the cascade. Finally, Kanani, et al. [23] predicts endwall heat transfer and secondary flows using wall-resolved LES at low and grid turbulence levels at an exit chord Reynolds number of 500,000. The predictions of Kanani are discussed here in this paper and qualitatively compared with the current endwall heat transfer measurements.

Experimental Approach

This experimental approach section includes a concise description of the cascade experiment (see Varty et al. [20] for a more complete description) and a more detailed description of the methodology used to acquire and process the visualizations generated by the infrared camera array. The present experiment was conducted using the wind tunnel presented in Fig. 1. The wind tunnel was designed to develop a uniform, low turbulence, constant temperature flow for cascade heat transfer and aero-loss experiments. The wind tunnel includes an inlet filter, a pressure blower, a two-stage multivane diffuser, a heat exchanger, a flow mixer and flow straightener, a screen box, and a 3.6 to 1 area ratio nozzle. The exit of the cascade attaches to a multivane diffuser for pressure recovery and flow redirection.

Cascade Wind Tunnel. The tunnel inlet consists of a filter box which holds eight large high-efficiency industrial filters. The blower, which entrains air from the filter box is driven by a variable frequency drive and can deliver up to 6.5 m^3/s of air at a static pressure rise of 5000 Pa. The blower discharges to a two-stage multivane diffuser, which distributes the airflow uniformly into the heat exchanger. The cooling water recirculation system for the heat exchanger includes a large mixing tank with controllable makeup and overflow. The airflow then moves into a coarse mixer to eliminate any temperature gradients in the flow. Subsequently, the flow is directed into a flow straighter and a series of four fine mesh screens to help remove any swirl and nonuniformities in the flow. The airflow then enters a smooth 3.6 to 1 area ratio nozzle which accelerates the flow, further reducing velocity nonuniformities, before entering the cascade test section.

Cascade Test Section. The cascade test section used to acquire the endwall heat transfer measurements is shown schematically in Fig. 2. This vane cascade is configured in a four-vane three full passage arrangement. The cascade inlet geometry includes bleed

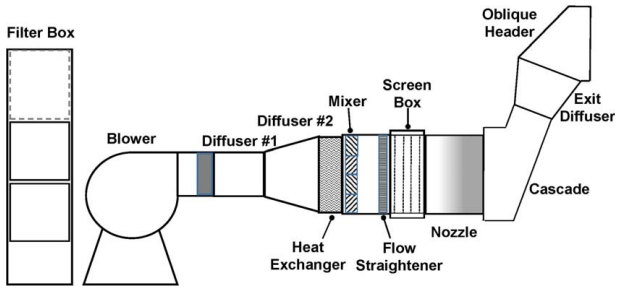

Fig. 1 Large-scale low-speed cascade wind tunnel with vane cascade

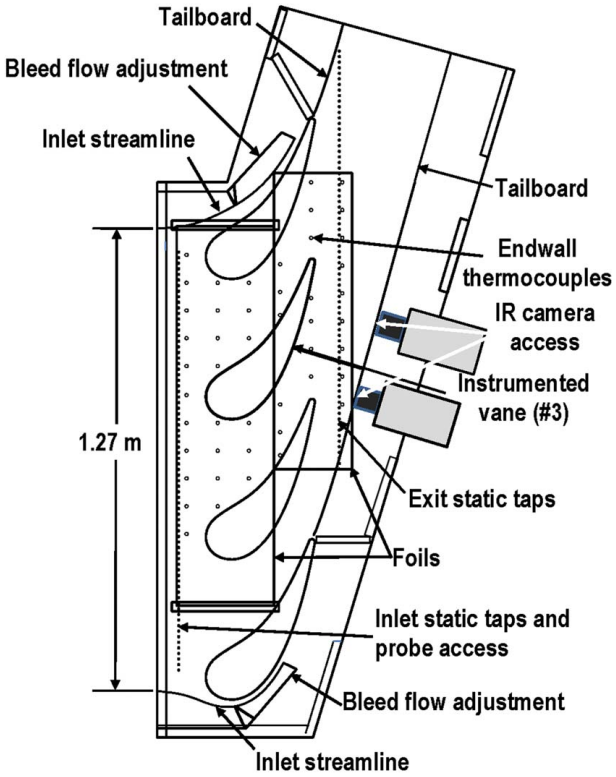

Fig. 2 Schematic of the large-scale linear vane cascade test section

flows above the top vane and below the bottom vane to help adjust the inlet flow uniformity. The cascade also includes adjustable tailboards which start at the trailing edge of the top and bottom vanes and extend to the exit. The cascade includes a row of inlet static pressure taps and exit static pressure taps to monitor and control inlet uniformity with the inlet bleeds and exit periodicity with the tailboards. The bleed flows and tailboards were initially set closely to streamlines based on periodic flow analysis and needed only minimal adjustment subsequently. The cascade sidewalls are fabricated from nominally 2.54 cm thick acrylic sheets. The far sidewall, shown schematically but not to proportion in Fig. 3, has two thin (23 μm) Inconel heater foils used to generate a constant heat flux. The Inconel foils are backed with a 50-μm Kapton film which in turn is backed with a thin high temperature acrylic adhesive. A 25 mm thick sheet of isocyanurate foam thermally insulates the heater foils. However, the entire far endwall surface is covered

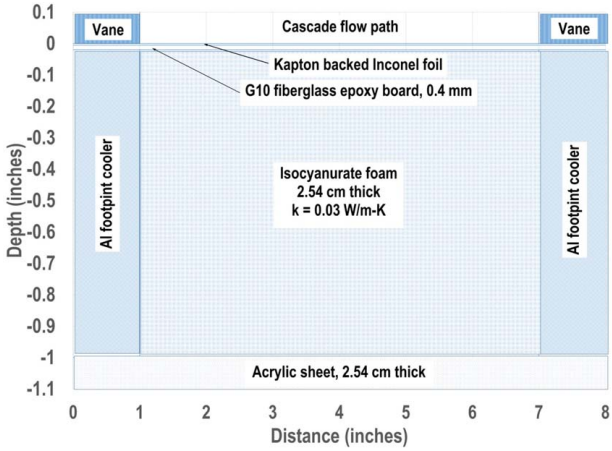

Fig. 3 Cross-sectional view of endwall construction

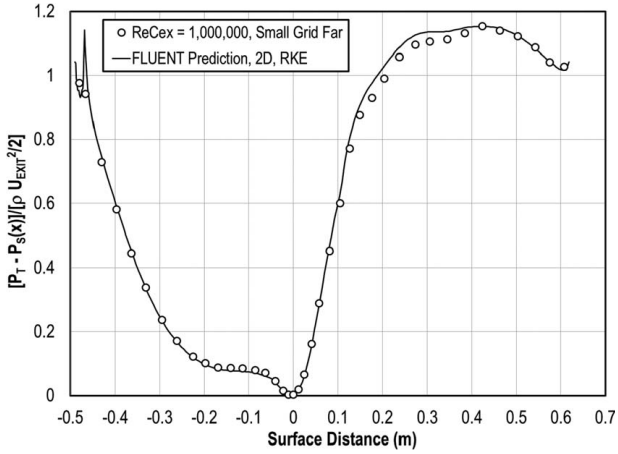

Fig. 4 Vane surface pressure distribution compared with blade-to-blade prediction, FLUENT

with 0.4 mm thick fiberglass epoxy board to ensure a smooth surface. The continuous Inconel foils are mounted on top of the fiberglass epoxy board. One issue related to the constant heat flux surfaces is the thermal energy, which is generated under the footprint of the vanes. In order to sink this unwanted thermal energy, footprint coolers in the shape of the vane profiles were fabricated and integrated into the foam under the vanes in the endwall. The footprint heat exchangers are cooled with air. The endwall also contains 47 fine wire (0.127 mm diameter) type K thermocouples epoxied into holes in the fiberglass epoxy board.

Instrumented Vanes. The cascade test section has a vane-shaped opening over the third vane from the bottom to allow for the insertion of instrumented vanes. Two vanes were used in the current testing including a vane to acquire the pressure distribution and a second vane designed to acquire the midspan surface heat transfer distribution. The vane design incorporates a relatively large leading edge to accommodate a double-wall cooling approach. The suction surface has been shaped to produce aft loading. The pressure profile shown in Fig. 4 compares the experimental measurements with the periodic solution for the vane. The profile initially shows a reasonably symmetrical acceleration around the stagnation line ($X = 0$). Over the near suction surface (positive surface distance) the acceleration is high but slower than what is typical. The minimum pressure occurs at around 70% of the suction surface distance followed by a moderate recovery to the trailing edge. The pressure surface (negative distance) indicates a very low acceleration just downstream from the stagnation point before a relatively rapid acceleration to the trailing edge. The vane leading edge diameter is about 13.2 cm at the stagnation point. The vane has a true chord is 49.8 cm and an axial chord of 28.4 cm. The circumferential spacing is 38.5 cm. The nominal turning angle is about 74 deg. The heat transfer vane was first used by Varty and Ames [19] and Varty et al. [20] and is described in those papers. However, in the present experiment, the heat transfer vane is simply used to generate a consistent heat transfer boundary condition with the endwall. Note that only the instrumented vane is heated while the others are adiabatic.

Turbulence conditions. Five inlet turbulence conditions with incremental intensities were developed to study their effect on endwall heat transfer and secondary flows. These conditions included the low turbulence (LT) condition (Tu = 0.7%), the small grid far (SGF) condition (Tu = 3.5%), the large grid (LG) condition (Tu = 7.9%), the aero-combustor (AC) condition (Tu = 12.6%), and the high turbulence aero-combustor (HT) condition (Tu = 17.4%). They are documented in Table 1 for the three

Table 1 Table of inlet turbulence conditions

	U (m/s)	Tu	Lx (cm)	Lu (cm)	ε (m^2/s^3)
HT	4.89	0.1744	3.76	6.66	13.95
	9.72	0.1744	3.91	7.22	101.3
	19.34	0.1718	4.00	7.69	715.9
AC	4.84	0.1235	3.68	7.24	5.61
	9.11	0.1302	3.52	6.36	42.1
	18.11	0.1259	3.58	7.35	253.4
LG	4.93	0.0755	2.00	3.27	2.13
	9.94	0.0790	2.04	3.35	23.4
	18.95	0.0813	2.35	3.53	163.4
SGF	4.70	0.0384	2.38	3.81	0.232
	9.08	0.0350	1.73	3.23	1.49
	17.61	0.0348	2.13	2.85	12.13
LT	4.96	0.0069	8.12	127	0.00005
	9.65	0.0076	5.02	154.5	0.00038
	18.71	0.0060	3.58	15.5	0.0139

Reynolds numbers chosen for the investigation. The low turbulence configuration is described in the cascade wind tunnel section and shown in Fig. 1. A picture of the nozzle used to develop this condition is presented in Fig. 5 on the left. The grid turbulence conditions are developed by adding a 0.914-m-long rectangular channel (shown on the right in Fig. 5) between the nozzle and the test section and placing one of two grids within. The SGF condition uses a square bar ($b = 0.635$ cm) square mesh ($M = 3.175$ cm) grid placed 32 mesh lengths upstream from the leading edge plane of the vanes. The large grid condition places a larger square bar ($b = 1.27$ cm) square mesh ($M = 6.35$ cm) grid (shown in Fig. 5) 10 mesh lengths upstream of the leading edge plane of the cascade vanes. The aero-combustor condition is developed by replacing the nozzle in the low turbulence configuration with the mock aero-combustor turbulence generator, shown schematically in Fig. 6, and is connected directly to the cascade. The high turbulence condition is similar in that this condition is generated by replacing the low turbulence nozzle with the high turbulence mock aero-combustor. The liner for the high turbulence mock aero-combustor is shown schematically in Fig. 7, and flow is directed through this liner in a manner similar to the mock aero-combustor (AC) shown in Fig. 6.

Fig. 5 A photo of the low turbulence (LT) 3.6 to 1 area contraction is shown on the left and a photo of the rectangular spool with the large grid (LG) is shown on the right

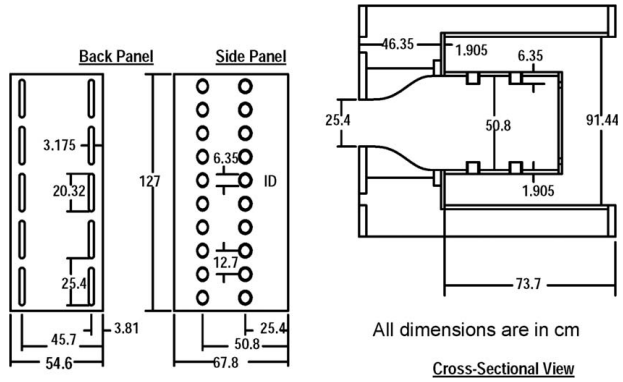

Fig. 6 Schematic of mock aero-combustor (AC) turbulence generator

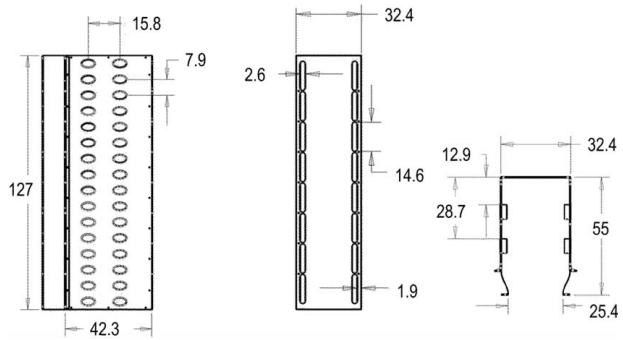

Fig. 7 Schematic of liner for high turbulence (HT) mock aero-combustor

Endwall Heat Transfer Measurements. Endwall heat transfer measurements were acquired using an array of small commercial infrared cameras manufactured by Therm-App. The Therm-App TH camera shown in Fig. 8 was used in the present investigation. This version of the camera was described as having a more accurate temperature measurement compared with the standard version. The camera has a resolution of 384 by 288 pixels with a sensitivity of 0.07 °C. The sensor array for the Therm-App camera is a microbolometer, which is reported to sense infrared wavelengths between 7.5 and 15 μm. The 6.8-mm lens is reported to provide a 55 deg by 41 deg viewing field.

Fig. 8 Therm-App infrared camera with 6.8-mm lens

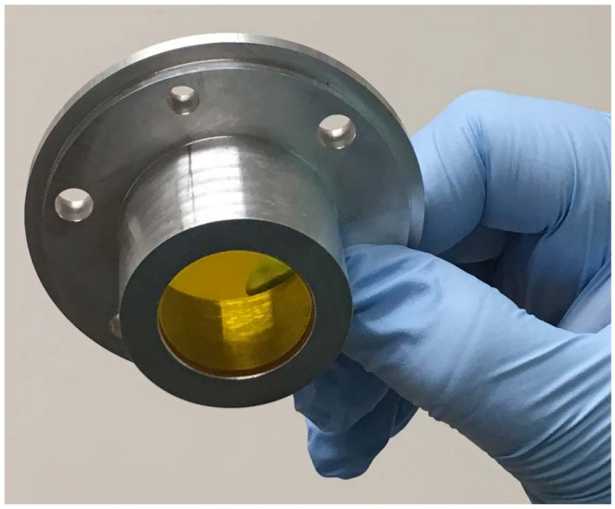

Fig. 9 Zinc selenide window for Therm-App camera

Issues relevant to applying an inexpensive commercial IR camera for measurements in this vane cascade included viewing area and placement, focal length, distortion, thermal droop, visual access, and calibration. Several different low-cost commercial cameras were reviewed including the Therm-App, the Seek Thermal, and the Flir ONE thermal cameras. The Therm-App camera had a few advantages including a design, which could be easily centered around a viewing window, a wide-angle lens which reduced the number of cameras needed, software which allowed downloading a *.csv file of temperatures, and a higher resolution. The Therm-App cameras have been designed to be used in combination with an android phone. The camera's software enables the user to set up, monitor, and acquire thermal images using the android phone controls. The infrared access was based on a 2.54-cm diameter coated zinc selenide window. The window holder shown in Fig. 9 was made from aluminum and was mounted in a 3.81-cm hole cut in the near cascade sidewall. The holder was bolted to the acrylic sidewall but adjusted to be flush with the inner endwall surface. The inside of the holder was large enough to accept the camera lens which sat about 1.63 cm from the inner surface of the endwall. The camera mount was developed in the shape of a cell phone, as shown in Fig. 10 and attached to the window holder's lip. An android cell phone was velcroed to the camera holder providing good visual access as well as access to the software control.

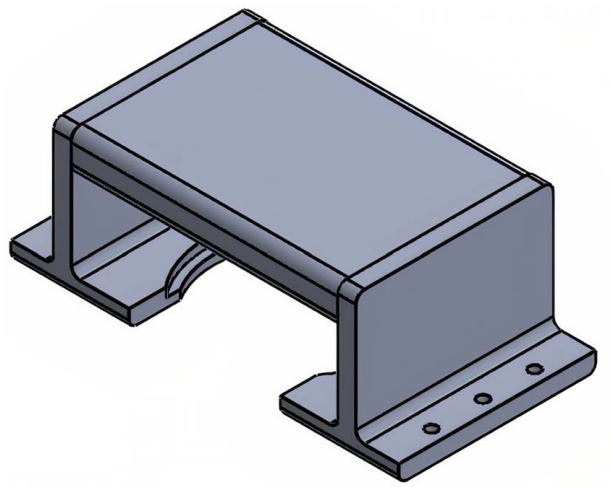

Fig. 10 Therm-App camera mount design

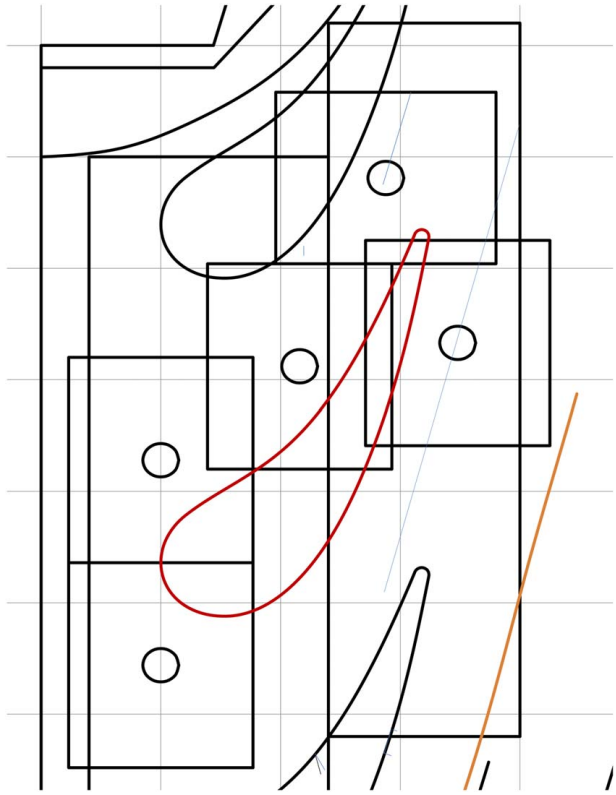

Fig. 11 Schematic of calculated camera coverage on endwall

The goal of endwall heat transfer measurements was to cover one entire endwall passage. Based on camera literature as well as experience with the camera during test and calibration, the area of coverage was estimated. That coverage was mapped out on the surface of the endwall as shown in Fig. 11. The resulting array of cameras is

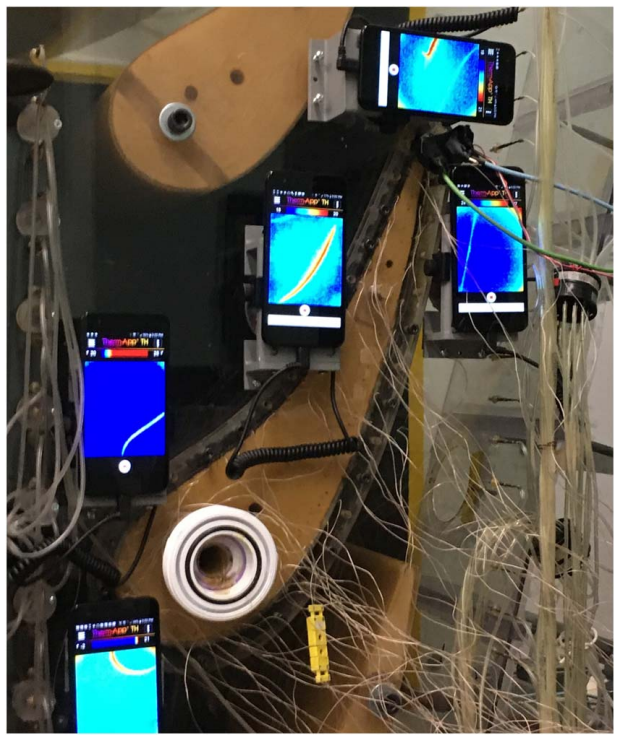

Fig. 12 Therm-App camera array mounted on endwall

shown mounted to the endwall in Fig. 12 numbered from 1 to 5 from bottom to top. Consequently, the furthest right camera is camera 4 and camera 5 is mounted perpendicular to the other cameras.

The cameras were adjusted for the fisheye effect and thermal droop at the edges, and they were all calibrated for sensitivity. A heated aluminum fixture with integrated type K thermocouples was used in the calibration of the cameras for sensitivity. The small microbolometers also had some edge effects which indicated lower temperatures than the central array. This thermal droop may have been due to some type of thermal losses near the edge of the array. Consequently, the effective calibration of the pixels at the edge was adjusted for this effect. Finally, due to the closeness of the sensor to the heat transfer surface, the thermal image is distorted. A comparison of the distorted image and the image compensated for the fisheye effect is shown in Fig. 13.

The data acquisition procedure began with the wind tunnel set at the proper exit chord Reynolds number for the given turbulence condition until the system reached steady-state. The system typically needed between 30 min and 1 h to achieve steady-state, depending on the Reynolds number. The wind tunnel Reynolds number and the adiabatic temperatures from the vane were recorded. Subsequent to starting data acquisition over the unheated test surface, thermal images from the five cameras were recorded. Afterward, a second set of thermocouple data and Reynolds number conditions were acquired. Next, power was applied across the two heater systems. Since the vane heater foil and the endwall heater foil are the same width as well as thickness, the same current was used for both. The aft endwall heater was set at the same heat flux as the forward heater using a second power supply. The system was allowed to reach steady-state limiting the maximum temperature on each endwall foil to 16 °C to 20 °C above the inlet temperature. Subsequently, flow conditions, thermocouple readings, and heater power readings were acquired at the steady-state condition and infrared images were recorded for the cameras. A followup dataset was also acquired. While some thermal drift is typical in the time between the adiabatic measurements and the heated measurements, small changes can be compensated for using the difference in the inlet total temperature readings between the heated and unheated cases.

Developing the temperature field for the endwall surface involved averaging the repeated images to reduce the pixel noise and then compensating for the fisheye effect and the thermal droop. The thermal field was then remapped into orthogonal coordinates. The individual adjoining images were then stitched together using a weighting scheme. The local Stanton number distribution was based on exit conditions and the local heated wall to adiabatic wall temperature difference while adjusting the heat flux for the local radiation loss. The simple estimate for radiation loss was determined using an emissivity of 0.95 for the painted black surface radiating to the local adiabatic temperature. The local adiabatic temperatures were adjusted for any thermal drift based on any changes in the inlet total temperature between adiabatic surface and heated surface runs.

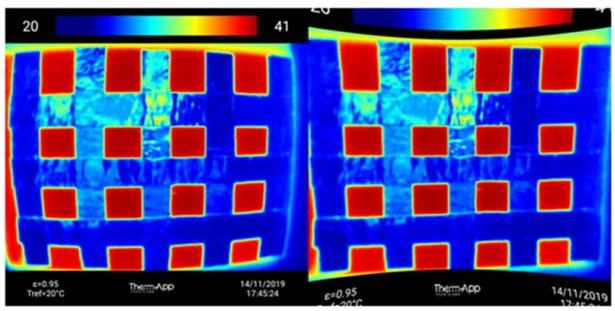

Fig. 13 Original image (left) corrected for fisheye affect (right)

Experimental Uncertainty Estimation. The experimental uncertainties in the values reported were estimated using the root sum square method described by Moffat [24]. The largest component of uncertainty in determining the Stanton number was due to the uncertainty in applying the temperature offset and individual gains to the individual cameras. The uncertainty in the reported Stanton number was as high as +/−12%. Other significant sources of uncertainty in the Stanton number include the uncertainty in the heat flux (+/−3%) and the uncertainty due to thermal drift (+/−2%). The uncertainty in the reported Reynolds number is estimated to be +/−1.5%, and the uncertainty in the reported pressure distribution is estimated to be +/−2%. The turbulence intensity and scale were determined using hot wire anemometry with uncertainties of +/−3% and +/−13%, respectively. All reported uncertainty values are based on a 95% confidence interval.

Experimental Results

Prior to acquiring any endwall heat transfer distributions, Kanani et al. [23] predicted endwall Stanton number distributions for the low turbulence and grid turbulence cases for the current cascade. His computations show some interesting features related to the endwall secondary flows. His LES computation for the low turbulence (LT) condition for the 500,000 chord exit Reynolds number is shown in Fig. 14. This figure shows two high heat transfer bands around the leading edge of the vane. The first high heat transfer band is attributed to the downwash of the leading edge horseshoe vortex and the band further out is attributed to a second vortex which Kanani calls the pressure side passage circulation (PPC) on the pressure side and the suction side passage circulation on the suction side of the leading edge. Just upstream of this outer high heat transfer region off the stagnation point and pressure surface, the location of the inlet boundary separation is expected to occur. This separation line has often been seen on old lampblack and oil flow visualizations. The line represents the extent to where upstream film cooling is expected to stay attached to the surface as well as noting the limiting location of the passage vortex.

Kanani's prediction for the large grid (LG) turbulence case shown in Fig. 15 is much different. The extent of this PPC off of the pressure surface is very much diminished as is the level of heat transfer along this secondary flow. This suggests that the

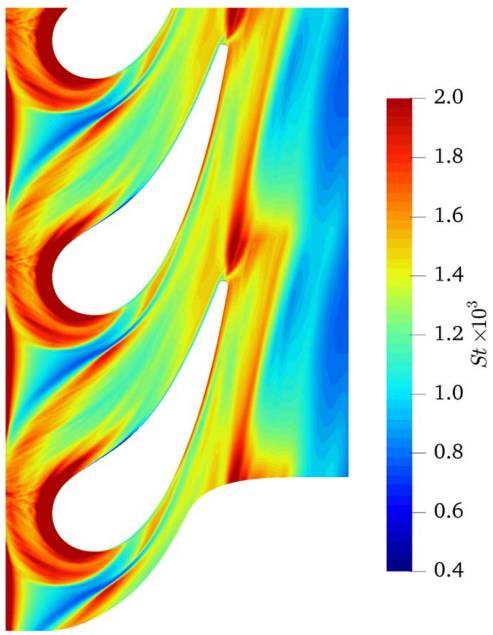

Fig. 14 LES predicted heat transfer contours, LT, $Re_C = 500{,}000$, Kanani et al. [23]

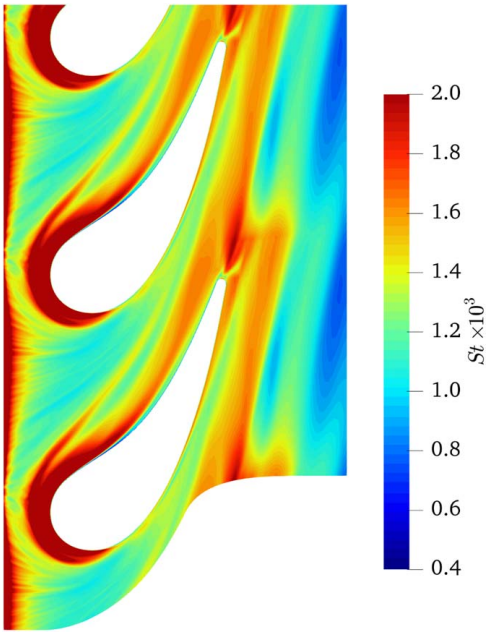

Fig. 15 LES predicted heat transfer contours, LG, Re_C = 500,000, Kanani et al. [23]

extent of the passage vortex for this vane cascade is significantly reduced. Potentially, this indicates that inflow turbulence has the potential to enhance the region of the endwall where film cooling protection can be effective.

Experimental Endwall Stanton Number Distributions. The experimental endwall Stanton number distribution based on exit conditions for the low turbulence case at a Reynolds number of 500,000 is shown in Fig. 16. This contour plot exhibits similar features to Kanani's predictions at the same condition. At the leading edge, a high heat transfer region directly upstream of the lead edge is present. The second high heat transfer band is also present and this band is well away from the leading edge and moves well off the pressure surface. Again, this PPC would indicate the extent of

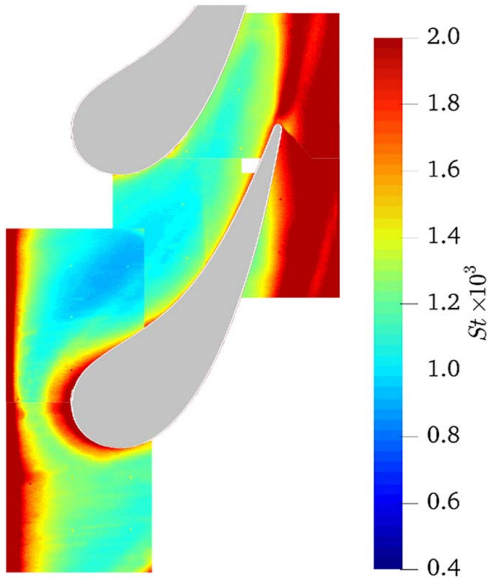

Fig. 17 Endwall Stanton number distributions, LG, Tu = 8.1%, Re_C = 500,000

the passage vortex as well as the inlet flow separation line. The region underneath the vane shows a PPC band that is even more prominent than the secondary flow above the vane. This higher level of heat transfer could be caused by the effect of the unheated lower vane or asymmetries in the flow expected with low vane count cascades.

The endwall Stanton number distribution for the large grid (LG) at an exit Reynolds number of 500,000 is presented in Fig. 17. This visualization shows some significant differences with the low turbulence case. Although a high heat transfer area around the leading edge is present, the extent of this region as well as the distinct nature of the second band is missing. You can see a very light indication of the extent of the pressure side passage circulation (PPC), and similar to Kanani's predictions, the location is much closer to the pressure side for this high turbulence case. Again, this location is expected to be the location of the inlet flow separation line and the

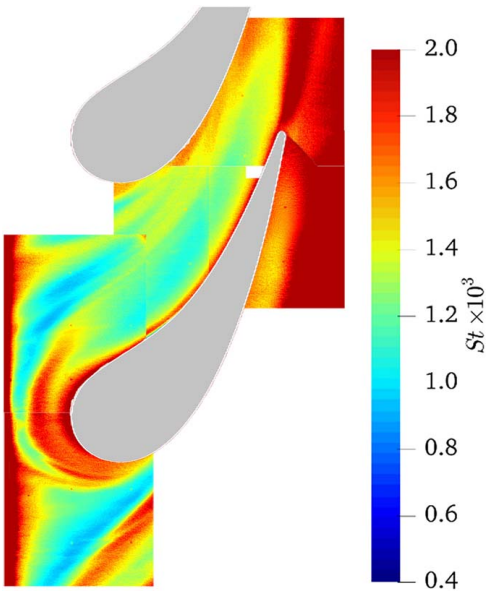

Fig. 16 Endwall Stanton number distributions, LT, Tu = 0.7%, Re_C = 500,000

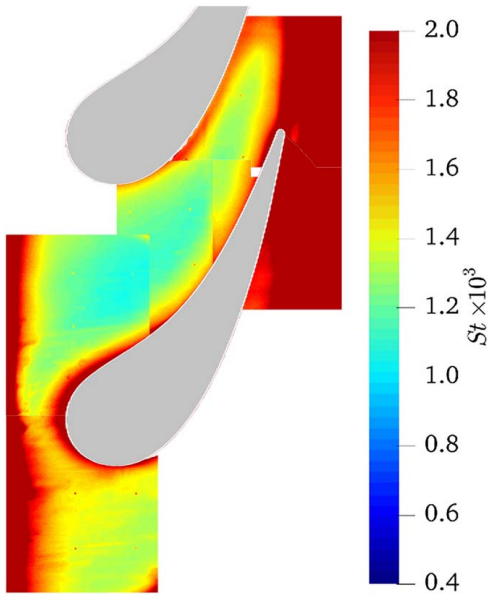

Fig. 18 Endwall Stanton number distributions, HT, Tu = 17.4%, Re_C = 500,000

region where film cooling protection will be swept away. In the middle of the passage, the heat transfer level appears to be low likely due to the lack of any secondary flow in this region.

The endwall Stanton number distribution for the high turbulence (HT) condition is presented in Fig. 18. Qualitatively the endwall heat transfer appears to be similar to the large grid in that no effects of secondary flows are discernable other than possibly at the leading edge where the high level of heat transfer indicates the influence of the flow downwash from the leading edge. However, in the passage, the heat transfer level appears to be roughly 20% higher than the large grid case. High turbulence typically reduces the extent of separation bubbles, produces a steeper near-wall velocity distribution, and tends to cause large-scale random unsteadiness. These processes are expected to reduce and wash out the effects of secondary flows.

Reynolds number is expected to have some effect on endwall Stanton number distributions. At higher Reynolds numbers boundary layers are typically thinner and skin friction coefficients and Stanton number levels are expected to decrease. Figure 19 presents endwall Stanton number distributions for the low turbulence condition at a Reynolds number of 1,000,000. Qualitatively, these endwall contours exhibit some similar features to the 500,000 Reynolds number low turbulence case. In the leading edge region, the double band of high heat transfer is evident. The passage vortex or PPC is evident off the pressure surface, especially in the view of camera one off the second vane in the cascade. There also appears to be a region of transition off the suction surface in the upper portion of the passage.

Endwall Stanton number distributions for the SGF at a Reynolds number of 1,000,000 is shown in Fig. 20. This figure shows similar features to the low turbulence case with the horseshoe vortex system which shows two bands of elevated heat transfer. The passage vortex or PPC line is quite discernable in this visualization providing an indication of the inlet separation line which is closer to the pressure surface than the low turbulence case. The heat transfer levels mid-passage appear low, fairly uniform, and similar in level to the low turbulence case.

The turbulence and inlet flow generated by the mock aero-combustor (AC) turbulence generator is expected to be representative of the inlet flow for a typical first-stage turbine nozzle. Figure 21 presents endwall Stanton number contours for this high turbulence case at an exit chord Reynolds number of 1,000,000. The influence of secondary flows is not apparent at this high turbulence. A small band of elevated heat transfer near the leading edge suggests the influence of the flow downwash

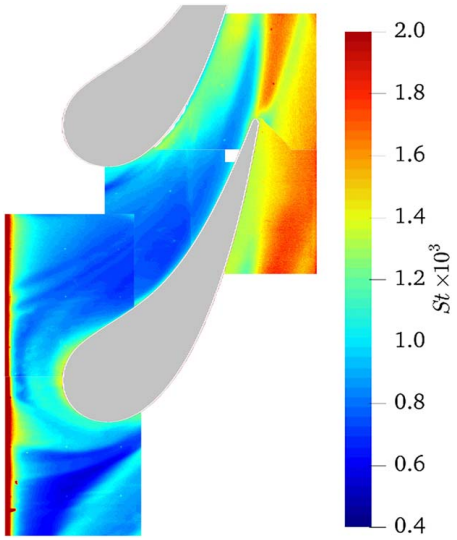

Fig. 19 Endwall Stanton number distributions, LT, Tu = 0.7%, Re_C = 1,000,000

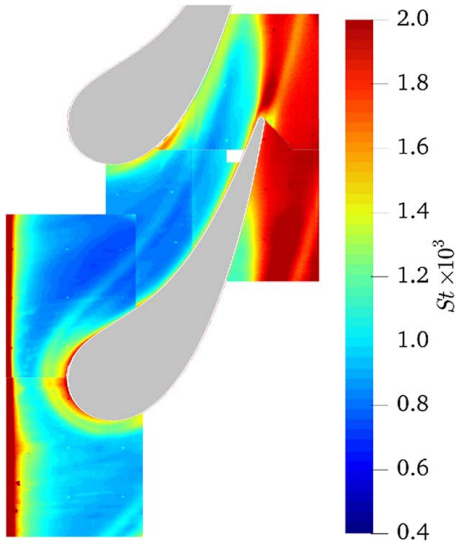

Fig. 20 Endwall Stanton number distributions, SGF, Tu = 3.5%, Re_C = 1,000,000

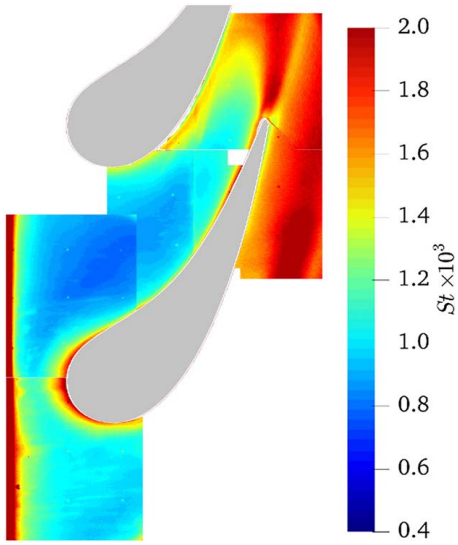

Fig. 21 Endwall Stanton number distributions, AC, Tu = 12.6%, Re_C = 1,000,000

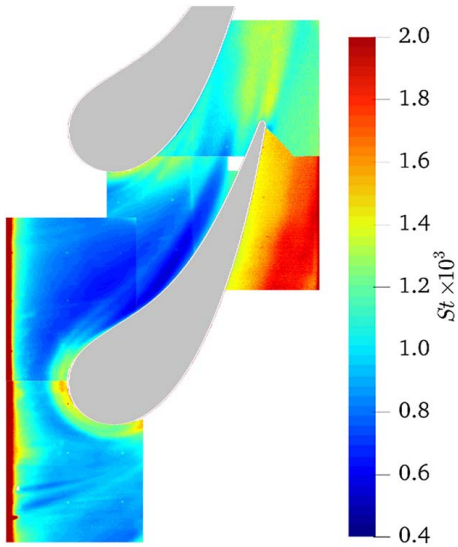

Fig. 22 Endwall Stanton number distributions, LT, Tu = 0.7%, Re_C = 2,000,000

Table 2 High, low and, average St no., $Re_C = 500{,}000$

Re_C	500,000					
Tu	LT	Camera 1	Camera 2	Camera 3	Camera 4	Camera 5
	High value	0.0055	0.0054	0.0018	0.0025	0.0032
	Low value	0.0003	0.0003	0.0003	0.0003	0.0004
	Average	0.0016	0.0015	0.0015	0.0017	0.0019
	Mid ave	0.0017	0.0014	0.0012	0.0016	0.0021
Tu	SGF	Camera 1	Camera 2	Camera 3	Camera 4	Camera 5
	High value	0.0062	0.0059	0.0020	0.0025	0.0025
	Low value	0.0010	0.0008	0.0009	0.0010	0.0011
	Average	0.0015	0.0015	0.0011	0.0015	0.0017
	Mid ave	0.0014	0.0015	0.0011	0.0013	0.0017
Tu	LG	Camera 1	Camera 2	Camera 3	Camera 4	Camera 5
	High value	0.0067	0.0065	0.0018	0.0026	0.0028
	Low value	0.0010	0.0009	0.0010	0.0010	0.0012
	Average	0.0016	0.0016	0.0012	0.0016	0.0018
	Mid ave	0.0016	0.0015	0.0011	0.0015	0.0022
Tu	AC	Camera 1	Camera 2	Camera 3	Camera 4	Camera 5
	High value	0.0071	0.0072	0.0022	0.0028	0.0030
	Low value	0.0011	0.0009	0.0010	0.0011	0.0015
	Average	0.0016	0.0017	0.0012	0.0017	0.0020
	Mid ave	0.0015	0.0014	0.0013	0.0013	0.0023
Tu	HT	Camera 1	Camera 2	Camera 3	Camera 4	Camera 5
	High value	0.0151	0.0138	0.0028	0.0033	0.0035
	Low value	0.0013	0.0010	0.0011	0.0012	0.0016
	Average	0.0021	0.0023	0.0014	0.0019	0.0024
	Mid ave	0.0019	0.0018	0.0014	0.0016	0.0025

off the vane. The heat transfer levels in the passage are moderately higher than for the two lower turbulence levels, and higher heat transfer is moving forward in the passage suggesting the possibility of the forward movement of transition. The boundary layer flow entering the cascade is expected to be transitional, (see Ames et al. [16]). However, the acceleration in the passageway is expected to be very high.

The highest exit chord Reynolds number of the current study was 2,000,000. The endwall Stanton number contours for the low turbulence case is shown in Fig. 22. At this highest Reynolds numbers, the double band of high heat transfer around the leading edge and off the pressure surface are still discernable. However, the extent of the pressure side passage circulation is much closer to the pressure surface than at the lower Reynolds numbers. The Stanton number level in the passage is visibly lower that the lower Reynolds numbers cases. However, the inlet boundary layer for this condition is expected to be turbulent. The highest levels of heat transfer for this condition can be seen off the

Table 3 High, low and, average St no., $Re_C = 1{,}000{,}000$

Re_C	1,000,000					
Tu	LT	Camera 1	Camera 2	Camera 3	Camera 4	Camera 5
	High value	0.0038	0.0040	0.0012	0.0019	0.0018
	Low value	0.0005	0.0007	0.0007	0.0008	0.0009
	Average	0.0010	0.0011	0.0009	0.0013	0.0015
	Mid ave	0.0010	0.0010	0.0009	0.0012	0.0013
Tu	SGF	Camera 1	Camera 2	Camera 3	Camera 4	Camera 5
	High value	0.0063	0.0052	0.0016	0.0024	0.0026
	Low value	0.0009	0.0007	0.0008	0.0008	0.0011
	Average	0.0013	0.0013	0.0010	0.0015	0.0018
	Mid ave	0.0010	0.0012	0.0008	0.0013	0.0019
Tu	LG	Camera 1	Camera 2	Camera 3	Camera 4	Camera 5
	High value	0.0053	0.0044	0.0012	0.0022	0.0022
	Low value	0.0008	0.0007	0.0007	0.0009	0.0011
	Average	0.0012	0.0012	0.0009	0.0014	0.0017
	Mid ave	0.0011	0.0010	0.0008	0.0012	0.0020
Tu	AC	Camera 1	Camera 2	Camera 3	Camera 4	Camera 5
	High value	0.0074	0.0026	0.0015	0.0024	0.0035
	Low value	0.0009	0.0008	0.0008	0.0010	0.0011
	Average	0.0014	0.0010	0.0010	0.0016	0.0018
	Mid ave	0.0013	0.0009	0.0009	0.0012	0.0019
Tu	HT	Camera 1	Camera 2	Camera 3	Camera 4	Camera 5
	High value	0.0061	0.0049	0.0016	0.0023	0.0037
	Low value	0.0009	0.0008	0.0008	0.0010	0.0011
	Average	0.0013	0.0011	0.0010	0.0015	0.0018
	Mid Ave	0.0013	0.0009	0.0009	0.0014	0.0018

Table 4 High, low, and average St no., $Re_C = 2{,}000{,}000$

Re_C	2,000,000					
Tu	LT	Camera 1	Camera 2	Camera 3	Camera 4	Camera 5
	High value	0.0088	0.0066	0.0028	0.0016	0.0028
	Low value	0.0008	0.0005	0.0005	0.0007	0.0008
	Average	0.0012	0.0012	0.0009	0.0011	0.0016
	Mid Ave	0.0009	0.0007	0.0007	0.0013	0.0015
Tu	SGF	Camera 1	Camera 2	Camera 3	Camera 4	Camera 5
	High value	0.0037	0.0041	0.0013	0.0020	0.0021
	Low value	0.0007	0.0006	0.0006	0.0008	0.0008
	Average	0.0009	0.0010	0.0008	0.0014	0.0015
	Mid Ave	0.0007	0.0006	0.0006	0.0012	0.0016
Tu	LG	Camera 1	Camera 2	Camera 3	Camera 4	Camera 5
	High value	0.0037	0.0035	0.0012	0.0018	0.0021
	Low value	0.0006	0.0006	0.0007	0.0008	0.0007
	Average	0.0010	0.0009	0.0009	0.0013	0.0014
	Mid Ave	0.0007	0.0006	0.0007	0.0014	0.0015
Tu	AC	Camera 1	Camera 2	Camera 3	Camera 4	Camera 5
	High value	0.0038	0.0042	0.0013	0.0020	0.0025
	Low value	0.0007	0.0006	0.0007	0.0008	0.0008
	Average	0.0010	0.0011	0.0009	0.0014	0.0015
	Mid Ave	0.0007	0.0007	0.0008	0.0012	0.0016
Tu	HT	Camera 1	Camera 2	Camera 3	Camera 4	Camera 5
	High value	0.0059	0.0055	0.0016	0.0022	0.0031
	Low value	0.0008	0.0007	0.0008	0.0010	0.0008
	Average	0.0012	0.0012	0.0010	0.0015	0.0016
	Mid Ave	0.0008	0.0007	0.0008	0.0013	0.0018

suction surface and downstream near the trailing edge off the pressure surface.

Analytical Assessment. The influence of secondary flows, turbulence level, and Reynolds number has been discussed in reasonable depth. However, these qualitative results provide little indication of the quantitative influence of these factors on endwall heat transfer. Tables 2–4 have been included to provide quantitative information on the high, low, average, and mid-average Stanton number for each camera and each condition. Table 2 tabulates the results of each camera for an exit chord Reynolds number of 500,000. Tables 3 and 4 list results for exit chord Reynolds numbers of 1,000,000 and 2,000,000 respectively. The high value is taken as the ninety-eighth percentile while the low value is the lowest small region of values in the camera view. The high values for cameras 1 and 2 were from the beginning of heating at the inlet of the cascade. The average value includes the average of all pixels in the camera view while the mid-average value focuses on a relatively constant value region within the camera view which qualitatively best represents the regional heat transfer level. This region is typically outside of significant secondary flows and unheated entry-length regions.

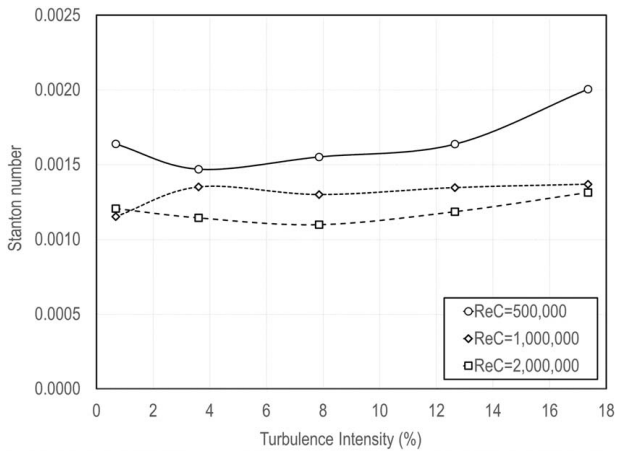

Fig. 23 Influence of turbulence intensity and Reynolds number on average endwall Stanton number

A five-camera average value for each condition was assessed for its Reynolds number dependence. The dependencies ranged from Reynolds number exponents of −0.18 to −0.30 with an average of −0.238. Additionally, these averaged values were plotted as a function of turbulence intensity and Reynolds number, and they are shown in Fig. 23. The Reynolds number dependence is readily apparent as the highest values are exhibited for the lowest Reynolds numbers. The trends with turbulence intensity are interesting. The averaged Stanton numbers for the lowest turbulence levels are higher than the SGF turbulence conditions. Previous investigators such as Gregory-Smith and Cleak [25] found that 5% grid-generated turbulence resulted in a 7% increase in profile losses but a 12% decrease in endwall losses. Although aerodynamic losses and heat transfer are not totally analogous, turbulence is known to reduce the extent of separated flows resulting in lower heat transfer in the region of reattachment. Generally, the averaged results show good consistency except for the low turbulence condition at a Reynolds number of 1,000,000.

Summary and Conclusions

This paper presents highly resolved experimental endwall Stanton number distributions at three Reynolds numbers and five widely varying turbulence levels. These experimental data were acquired using an array of five high-resolution infrared cameras. The experimental data at the lowest Reynolds number were compared to highly resolved LES calculations showing some good consistency qualitatively. The authors believe that the present data will be very useful in grounding computational methods for the prediction of endwall heat transfer.

Secondary flows are very discernable in the heat transfer visualizations at the lower levels of turbulence. These distributions evidence the character of the leading edge horseshoe vortex system

as well as the movement of the passage vortex or PPC. The horseshoe vortex system including the passage vortex is clearly influenced by both Reynolds number and turbulence. The strength and extent of the horseshoe vortex system near the leading edge notably wanes with increasing Reynolds number. Evidence of two bands of high heat transfer which might be attributed to the downwash of the horseshoe vortex and possibly the secondary or tertiary vortex appear significantly diminished with elevated turbulence.

The endwall area upstream of the inlet boundary separation line may be a good indication of the region where inlet film cooling may be sustained. Experimental evidence of the location of the passage vortex or PPC shows that it moves much closer to the pressure surface with increasing turbulence levels and to a lesser extent increasing Reynolds numbers. This may suggest inlet film cooling may persist well onto the endwall surface for some designs at higher turbulence levels and or Reynolds numbers.

Acknowledgment

The authors would like to express appreciation to the University of North Dakota for helping to support the present work. The authors are also grateful to the senior design team which helped significantly with the current project.

Conflict of Interest

There are no conflicts of interest.

Data Availability Statement

The data sets generated and supporting the findings of this article are obtainable from the corresponding author upon reasonable request.

Nomenclature

h = heat transfer coefficient, W/m^2/K
C = true chord length, m
P = pressure, Pa
T = Temperature, K
C_P = specific heat at constant pressure, J/kg/K
U_∞ = free-stream velocity, m/s
Lu = energy scale of turbulence, $Lu = 1.5\ |u'|^3/\varepsilon$
Lx = longitudinal integral scale of turbulence, m
Re_C = chord Reynolds number based on exit conditions
St = Stanton number, $St = h/\rho\ U_{EXIT}\ C_P$
Tu = local turbulence level, u'/U_∞
u', $|u'|$ = streamwise component of rms fluctuation velocity

Greek Symbols

ε = turbulent dissipation
ρ = density, kg/m^3

Subscripts

EXIT = referenced to vane exit conditions
S = static condition
T = total condition

References

[1] Sieverding, C. H., 1985, "Recent Progress in the Understanding of Basic Aspects of Secondary Flow in Turbine Blade Passages," ASME J. Eng. Gas Turbines Power, **107**(2), pp. 248–257.
[2] Klein, A., 1966, ''Investigation of the Entry Boundary Layer on the Secondary Flows in the Blading of Axial Turbines,'' BHRA T 1004.
[3] Langston, L. S., Nice, M. L., and Hooper, R. M., 1977, "Three-Dimensional Flow Within a Turbine Cascade Passage," ASME J. Eng. Power, **99**(1), pp. 21–28.
[4] Graziani, R. A., Blair, M. F., Taylor, J. R., and Mayle, R. E., 1980, "An Experimental Study of Endwall and Airfoil Surface Heat Transfer in a Large Scale Turbine Blade Cascade," J. Eng. Power, **102**(2), pp. 257–267.
[5] Marchal, P., and Sieverding, C. H., 1977, ''Secondary Flows Within Turbomachinery Bladings,'' Secondary Flows in Turbomachines, AGARD CP 214.
[6] Langston, L. S., 2006, "Secondary Flows in Axial Turbines—A Review," Ann. N. Y. Acad. Sci., **934**(1), pp. 11–26.
[7] Sharma, O. P., and Butler, T. L., 1987, "Predictions of End-Wall Losses and Secondary Flows in Axial flow Turbine Cascades," ASME J. Turbomach., **109**(2), pp. 229–236.
[8] Goldstein, R. J., and Spores, R. A., 1988, "Turbulent Transport on the Endwall in the Region Between Adjacent Turbine Blades," J. Heat Transf., **110**(4a), pp. 862–869.
[9] Wang, H. P., Olson, S. J., Goldstein, R. J., and Eckert, E. R. G., 1997, "Flow Visualization in a Linear Turbine Cascade of High Performance Turbine Blades," ASME J. Turbomach., **119**(1), pp. 1–8.
[10] Praisner, T. J., and Smith, C. R., 2006, "The Dynamics of the Horseshoe Vortex and Associated Endwall Heat Transfer, Part I—Temporal Behavior," ASME J. Turbomach., **128**(4), pp. 747–754.
[11] Praisner, T. J., and Smith, C. R., 2006, "The Dynamics of the Horseshoe Vortex and Associated Endwall Heat Transfer, Part II—Time Mean Results," ASME J. Turbomach., **128**(4), pp. 755–762.
[12] York, R. E., Hylton, L. D., and Milelc, M. S., 1984, "An Experimental Investigation of Endwall Heat Transfer and Aerodynamics in a Linear Vane Cascade," ASME J. Eng. Gas Turbines Power, **106**(1), pp. 159–167.
[13] Harasgama, S. P., and Wedlake, E. T., 1989, "Heat Transfer and Aerodynamics of a High Rim Speed Turbine Nozzle Guide Vane Tested in the RAE Isentropic Light Piston Cascade," ASME J. Turbomach., **113**(3), pp. 384–391.
[14] Spencer, M. C., Jones, T. V., and Lock, G. D., 1996, "Endwall Heat Transfer Measurements in an Annular Cascade of Nozzle Guide Vanes at Engine Representative Reynolds and Mach Numbers," Int. J. Heat Fluid Flow, **17**(2), pp. 139–147.
[15] Radomsky, R., and Thole, K. A., 2000, "High Freestream Turbulence Effects in the Endwall Leading Edge Region," ASME J. Turbomach., **122**(4), pp. 699–708.
[16] Ames, F. E., Barbot, P. A., and Wang, C., 2003, "Effects of Aeroderivative Combustor Turbulence on Endwall Heat Transfer Distributions Acquired in a Linear Vane Cascade," ASME J. Turbomach., **125**(2), pp. 210–220.
[17] Ames, F. E., Barbot, P. A., and Wang, C., 2005, "Effects of Catalytic and Dry Low NOx Combustor Turbulence on Endwall Heat Transfer Distributions," ASME J. Heat Transfer., **127**(4), pp. 414–424.
[18] Giel, P. W., Thurman, D. R., Van Fossen, G. J., and Boyle, R. J., 1998, "Endwall Heat Transfer Measurements in a Transonic Turbine Cascade," ASME J. Turbomach., **120**(2), pp. 305–313.
[19] Varty, J. W., and Ames, F. E., 2016, "Experimental Heat Transfer Distributions Over an Aft Loaded Vane With a Large Leading Edge at Very High Turbulence Levels," ASME IMECE, Paper No. IMECE2016-67029.
[20] Varty, J. W., Soma, L. W., Ames, F. E., and Acharya, S., 2017, "Vane Suction Surface Heat Transfer in Regions of Secondary Flows: The Influence of Turbulence Level, Reynolds Number, and the Endwall Boundary Condition," ASME J. Turbomach., **140**(2), p. 021010.
[21] Kanani, Y., Acharya, S., and Ames, F. E., 2019, "Large Eddy Simulation of the Laminar Heat Transfer Augmentation on the Pressure Side of a Turbine Vane Under Freestream Turbulence," ASME J. Turbomach., **141**(4), p. 041004.
[22] Kanani, Y., Acharya, S., and Ames, F. E., 2020, "Large Eddy Simulation of Bypass Transition in Vane Passage With Freestream Turbulence," ASME J. Turbomach., **142**(6), p. 061002.
[23] Kanani, Y., Acharya, S., and Ames, F. E., 2021, "Numerical Predictions of Turbine Cascade Secondary Flows and Heat Transfer With Inflow Turbulence," ASME J. Turbomach., **143**(12), p. 121008.
[24] Moffat, R. J., 1988, "Describing the Uncertainties in Experimental Results," Exp. Therm. Fluid Sci., **1**(1), pp. 3–17.
[25] Gregory-Smith, D. G., and Cleak, J. G. E., 1992, "Secondary Flow Measurements in a Turbine Cascade With High Inlet Turbulence," ASME J. Turbomach., **114**(1), pp. 173–183.